

Investigation of the Hot Deformation Behavior in VDM® Alloy 780 by *In Situ* High-Energy X-Ray Diffraction



MASSIMO FRITTON, FRANK KÜMMEL, ANDREAS KIRCHMAYER, ANDREAS STARK, MASOOD HAFEZ HAGHIGHAT, BODO GEHRMANN, STEFFEN NEUMEIER, and RALPH GILLES

Ni-based superalloys are indispensable for applications in demanding environments, such as the heavily stressed rotating discs in the hot sections of modern gas turbines or jet engines. In this paper, the microstructure evolution during hot deformation to mimic the forging process was investigated in the polycrystalline VDM® Alloy 780 *via in situ* X-ray diffraction at temperatures of 950, 1000, and 1050 °C. For the tested temperatures, the hot forming led to subgrain formation, the built-up of a texture by rotation of the matrix grains into preferred orientations, and dynamic recrystallization. The influence of the deformation was analyzed depending on the direction of the lattice plane normals to the load direction, for the first five γ -reflections in the diffraction pattern. During uniaxial compressive deformation intensity, maxima develop in the loading direction solely for the γ -(220) reflections, while intensity minima develop for the other reflections which correspond to the formation of a $\langle 110 \rangle$ fiber texture. In the transverse direction, all γ -reflections except the (220) have an increased intensity at the maximum specimen strain of 20 pct. Directly after the hot forming, three different cooling rates of 10, 100, and 1000 °C/min and their influence on the microstructure were investigated. The fast and medium cooling rates lead to low recrystallized fractions and a largely preserved deformation texture, whereas the low cooling rate leads to a high recrystallized fraction and a slight remaining texture. Additionally, the diffraction data are complemented by electron microscopy measurements.

<https://doi.org/10.1007/s11661-022-06942-5>
© The Author(s) 2023

I. INTRODUCTION

POLYCRYSTALLINE Ni-based superalloys are used as components of gas turbine engines for onshore power generation and aircraft propulsion due to their good mechanical properties at high temperatures and their resistance to corrosive or oxidizing conditions.^[1,2] A particularly important aspect is to further increase the

maximum application temperatures in order to reduce fuel consumption, *i.e.*, to increase efficiency and reduce CO₂ emission. Alloy 718 is the most commonly used Ni-based superalloy as it combines unique mechanical properties and good processing characteristics, but its maximum application temperature is limited to about 650 °C. The new VDM® Alloy 780 is a Ni-based superalloy developed for higher service temperatures than the widely used alloy 718, comprising γ matrix (Ni-based, Al crystal structure), γ' hardening phase (Ni₃Al-based, L1₂ crystal structure), and δ (Ni₃Nb-based, DO_a) and η (Ni₃Ti-based, DO₂₄) high-temperature (HT) phases.^[3–5] The main differences compared to alloy 718 are mainly the substitution of Fe and Ni by Co and a higher Al content in combination with a lower Ti content. The increased Al content and diminished Ti content lead to a more stable γ' phase, while Co is used because it limits the solvus temperature of the γ' phase despite the high aluminum content and stabilizes the δ phase.^[6] This facilitates the formation of a stable γ' phase with comparatively low solvus temperature and prevents the precipitation of metastable γ'' . In alloy 718,

MASSIMO FRITTON, FRANK KÜMMEL, and RALPH GILLES are with the Heinz Maier-Leibnitz Zentrum, Technische Universität München, 85748, Garching, Germany. Contact e-mail: Massimo.Fritton@frm2.tum.de ANDREAS KIRCHMAYER and STEFFEN NEUMEIER are with the Lehrstuhl für Werkstoffwissenschaften, Friedrich-Alexander-Universität Erlangen-Nürnberg, 91058, Erlangen, Germany. ANDREAS STARK is with the Metallphysik, Helmholtz-Zentrum hereon GmbH, 21502, Geesthacht, Germany. MASOOD HAFEZ HAGHIGHAT and BODO GEHRMANN are with the VDM Metals International GmbH, 65439, Frankfurt am Main, Germany.

Manuscript submitted August 1, 2022; accepted December 21, 2022.

Article published online January 16, 2023

the transformation of γ'' into the brittle δ phase sets in around 650 °C, explaining why its service temperature is limited. For Alloy 718, the microstructure evolution during hot forming and the precipitation of the hardening phases were investigated by theoretical as well as experimental studies.^[7,8] The very good mechanical strength of VDM® Alloy 780 at high temperatures can be largely attributed to its characteristic two-phase microstructure, in which the γ' -precipitates are coherently embedded in the γ -matrix and exhibit a high lattice misfit.^[6] For the mechanical properties, more precisely the creep resistance, a high γ/γ' lattice mismatch together with a high volume fraction of γ' is beneficial at application temperatures of about 750 °C.^[9,10] The presence of the different phases and the quantity, shape, and size of the various precipitates depend on the chemical composition, processing conditions, and heat treatments. The microstructure of the alloy has already been characterized in detail by *in situ* measurements and after various heat treatments by the authors of this publication *via* neutron diffraction (ND), small-angle neutron scattering (SANS), scanning electron microscopy (SEM), and high-resolution transmission electron microscopy (HRTEM).^[3–5] Thereby, the lattice parameters of the matrix and hardening phase and the resulting lattice mismatch, which is crucial for the mechanical properties, were determined from RT to the solvus temperature of γ' at around 970 °C. Additionally, also the volume fractions, shape, and average grain sizes were determined by the combination of the above-mentioned techniques. In a recent publication by Kümmel *et al.*, VDM® Alloy 780 specimens were investigated *in situ* at RT and elevated temperatures under uniaxial tensile deformation.^[11] The deformation, which is mainly dislocation motion and shearing of the γ precipitates, was found to be anisotropic and dependent on the grain orientation.^[11] Supersolvus forging of VDM® Alloy 780 specimens was already investigated by Sharma *et al.* where the dynamic recrystallization (DRX) was a central aspect of the study.^[12] They observed an increased dynamically recrystallized fraction with increasing strain level and deformation temperature and a higher dynamically recrystallized fraction for the lower strain rate. For the two applied strain rates of 0.1 s⁻¹ and 0.01 s⁻¹ and strain levels (0.4 to 1.3), similar grain sizes were observed for a given temperature.^[12] Additionally, they observed slower grain growth kinetics as compared to Alloy 718, which can be an advantage, since finer grain sizes after forging in the single-phase domain can be obtained.^[12] To date, however, there is no *in situ* diffraction study of this alloy at high temperatures and compressive deformation to investigate the evolution of the microstructure. A major advantage of the *in situ* XRD measurements in the current work is that the development of the microstructure can be observed non-destructively in real time during the forging process and not only after a cooling and sample preparation process, which also changes the microstructure of the sample. The formation and evolution of the texture are studied with increasing deformation for the first five γ -reflections in the diffraction pattern: (111), (200), (220), (311), and

(222). These measurements are used, for example, to directly observe the rotation of individual grains (c.f. Figure 5), but also to draw conclusions on the formation of small-angle grain boundaries, *i.e.*, subgrain formation. The properties, such as peak intensity, full width at half maximum (FWHM), position, and their evolution with increasing deformation can be studied here for lattice plane normals in the loading direction or *perpendicular* to it (transverse direction) (c.f. Figure 9). Furthermore, *via* the analysis of the individual diffraction rings, conclusions can be drawn about the grain size development and the formation of a texture with increasing deformation (c.f. Figure 6). The experiments provided information about the material behavior during the forging and cooling process, which is an important aspect for further optimization of the microstructure during the manufacturing process.

II. MATERIALS AND METHODS

The chemical composition of the investigated samples is given in Table I. The starting material from the same batch for all experiments presented in this publication was treated identically as follows: 1080 °C/1 h/WQ, where WQ = water quenching. The heat treatment leads to a fully recrystallized microstructure with no preferred orientation and average grain sizes of approximately 70 μm (c.f. Figure 13(a)). Since the precipitation of γ' is to be investigated later in a separate publication and the forging process is to be studied in the single-phase region, a temperature program was selected to prevent premature precipitation of γ' . Since no γ' superstructure reflections are visible in the diffractogram (see electronic supplementary Figure S1), only tiny amounts of less than one vol pct could be present.

Cylindrical samples with a length of 10 mm and a diameter of 5 mm were used for the *in situ* high-energy XRD experiments. The diffraction patterns were recorded at the HEMS^[13] beamline at PETRA III, DESY (Hamburg, Germany) using X-rays with a wavelength of 0.124 Å, *i.e.*, a photon energy of 100 keV. A spot size of 1 mm² of the X-ray beam on the sample leads to an illuminated sample volume of approximately 5 mm³. XRD patterns were recorded using a flat panel detector (XRD1621, Perkin Elmer, Norwalk, CT, USA) with acquisition rates up to 5 HZ, a pixel size of (200) × (200) μm^2 , and a resolution of 2048 × 2048 pixels. The detector was positioned with a distance of 1630 mm between the sample and the detector, and the primary beam impinged on the center of the detector so that complete Debye-Scherrer rings were recorded. By using the quenching and deformation dilatometer (DIL 805A/D, TA Instruments, Hüllhorst,

Table I. Chemical Composition of VDM® Alloy 780 Determined by EDX Measurements

	Ni	Co	Cr	Fe	Mo	Nb	Al	Ti
wt pct	45.5	25.5	18	0.6	2.8	5.1	2	0.4

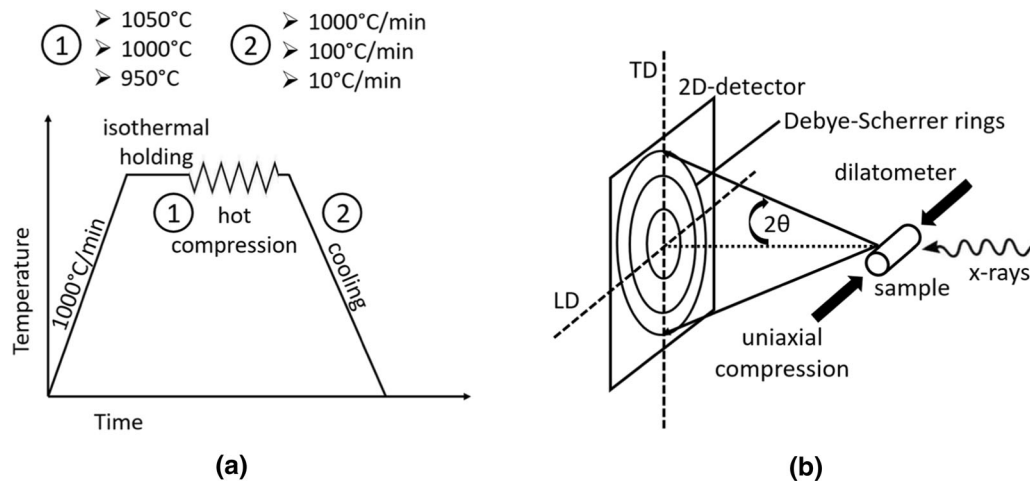


Fig. 1—(a) Scheme of the performed forging experiments and (b) experimental setup for the diffraction experiments with load direction (LD) and transverse direction (TD).

Germany),^[14] defined heating and cooling of the specimens at rates of 1000 °C/min was possible, with simultaneous deformation of the specimens. The dilatometer is equipped with a hydraulic compression device and the distance between the two Si₃N₄ stamps is measured by a displacement transducer (LVDT).

To minimize sample oxidation, the experiments were performed in an Ar atmosphere. The temperature was controlled *via* spot-welded type S thermocouples. Figure 1 schematically shows the experimental procedure and setup.

The specimens were heated up to the deformation temperatures of 950, 1000, and 1050 °C with 1000 °C/min and kept for approximately one minute to ensure temperature homogeneity and were then compressed with a deformation rate of $1 \times 10^{-3} \text{ s}^{-1}$ to about 20 pct height reduction. Subsequently, the specimens were cooled down to 500 °C with three different cooling rates (10, 100, and 1000 °C/min) by defined blowing with Ar gas. Below 500 °C, the samples were cooled down to 50 °C with a maximum cooling rate to save valuable experiment time since no changes in the microstructure occur below this temperature.

The high-energy X-ray diffraction (HEXRD) experiments were carried out in transmission geometry, which also explains the chosen photon energy mentioned above. The 2D raw data from the synchrotron measurements were treated with the software Fit2D (ESRF, Grenoble, France).^[15] Furthermore, the root-mean-square roughness (R_q) of the normalized intensity vs azimuthal angle was calculated according to the equation:^[16]

$$R_q = \sqrt{\frac{1}{N} \sum_{n=1}^N (I_n - \bar{I})^2} \quad [1]$$

I is the intensity at the respective angle, \bar{I} is the average intensity, and N defines the number of azimuthal angles investigated. The values were evaluated for the azimuthally unrolled (111) Debye-Scherrer ring. Coarse grains

lead to poor grain statistics and result in strongly varying intensity distribution along the diffraction rings, *i.e.*, high R_q values. Therefore, R_q can be considered as a measure of the number of grains in the illuminated volume. However, the formation of a texture also affects the R_q values due to the developing intensity minima and maxima.

Microstructural analysis was performed by using a scanning electron microscope (SEM) (Zeiss XB 540 Dualbeam) to determine the proportion of the recrystallized, substructured, and deformed area using back scattered diffraction (BSD) and electron backscatter diffraction (EBSD). The SEM samples were ground, polished to 1 μm, and afterward polished with a colloidal silica suspension. Both modes were used with an acceleration voltage of 20 kV and a working distance of 8.5 mm. For the EBSD images, a 70 deg sample holder and a detector from Oxford instruments were used. Whether the investigated area has been classified as “recrystallized,” “substructured,” or “deformed” depends on the internal misorientation angle within the grain. If the maximum misorientation angle found within a single grain exceeds 1 deg, the grain is classified as being “deformed.” Grains that consist of subgrains whose internal misorientation is below 1 deg but the misorientation from subgrain to subgrain is above 1 deg are classed as “Substructured.” All remaining grains are classified as “recrystallized.”

III. RESULTS AND DISCUSSION

In the first part of the results section, the evolution of the microstructure during hot compressive deformation is studied simultaneously by a combination of mechanical characterization and XRD. In the second part of the results, the influence of different cooling rates on the microstructure is investigated by XRD and SEM.

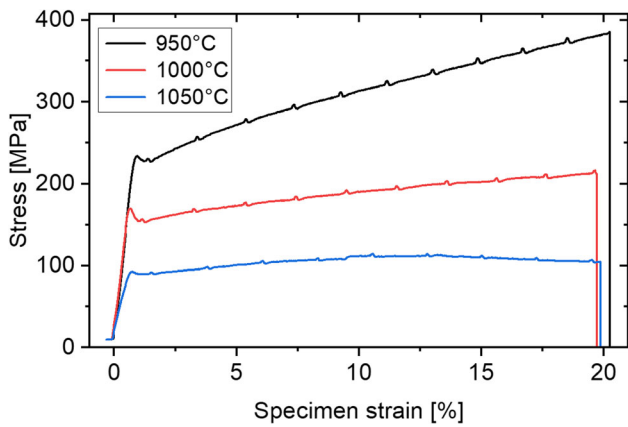


Fig. 2—Stress–strain curves for the specimens tested at 950 deg (black line), 1000 °C (red line), and 1050 °C (blue line) at deformation rates of $1 \times 10^{-3} \text{ s}^{-1}$ (Color figure online).

A. Microstructural Evolution During Hot Deformation

1. Deformation behavior

The influence of compressive deformation of VDM® Alloy 780 specimens and its effect on the microstructure is studied at temperatures of 950, 1000, and 1050 °C. To describe the forming behavior of the alloy, stress–strain diagrams are shown below, at the respective temperatures. The small regularly occurring spikes in the force values are an artifact of the hydraulics that occurs when deforming with the dilatometer.

When analyzing the rheological behavior, it is noticeable that the maximum force at the lowest temperature is more than three times higher than the force at the highest temperature. The solvus temperature of γ' is approximately 970 °C, and the solvus temperature of the η and δ high-temperature (HT) phases is in the range of 1020 °C.^[7] This may explain the significantly increased force to be applied for the test at 950 °C since

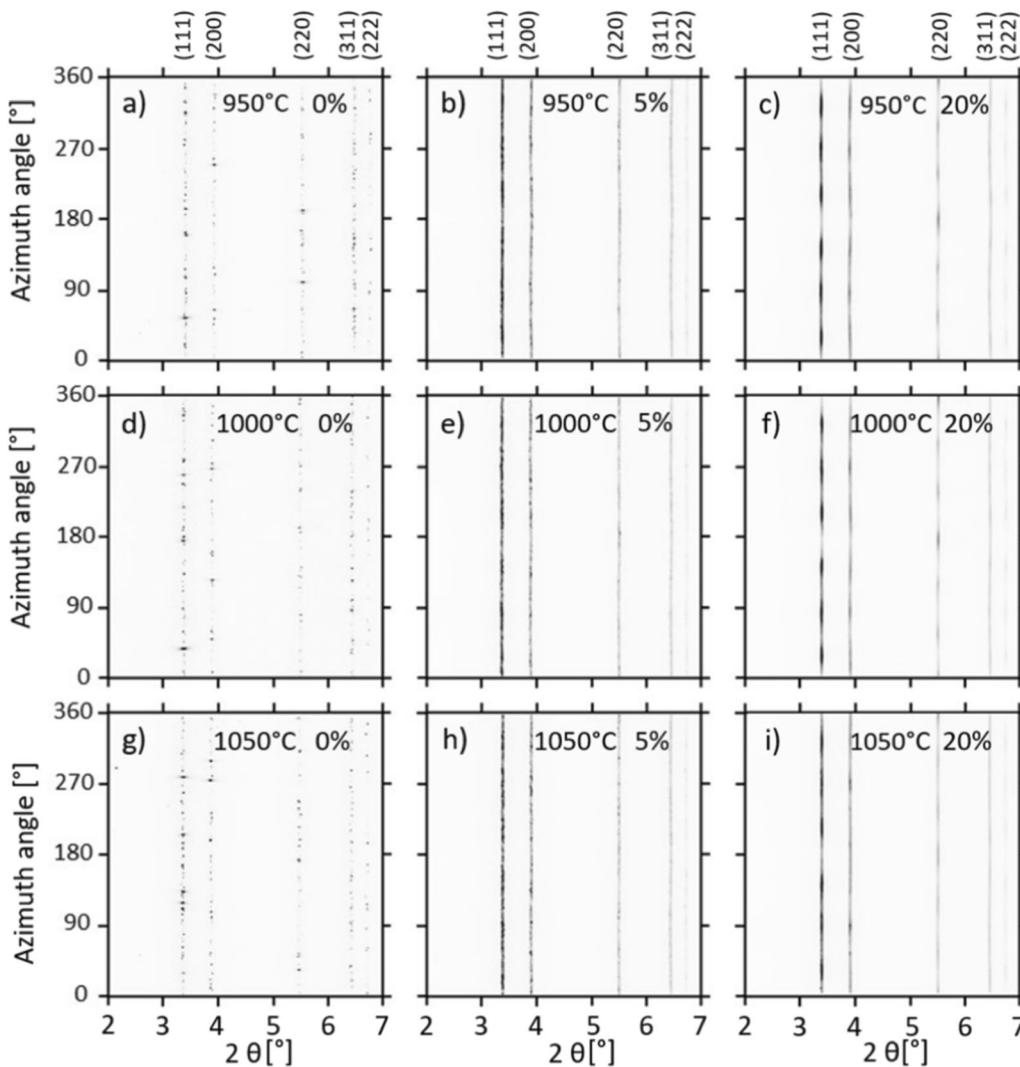


Fig. 3—Unrolled diffraction rings during hot forming experiments of VDM® Alloy 780 samples at (a) through (c) 950 °C, (d) through (f) 1000 °C, and (g), (h) 1050 °C; (a, d, g) before deformation, (b), (e), (h) 5 pct deformation, and (c), (f), (i) after 20 pct deformation. The reflections of the γ phase are depicted at the top of the figure.

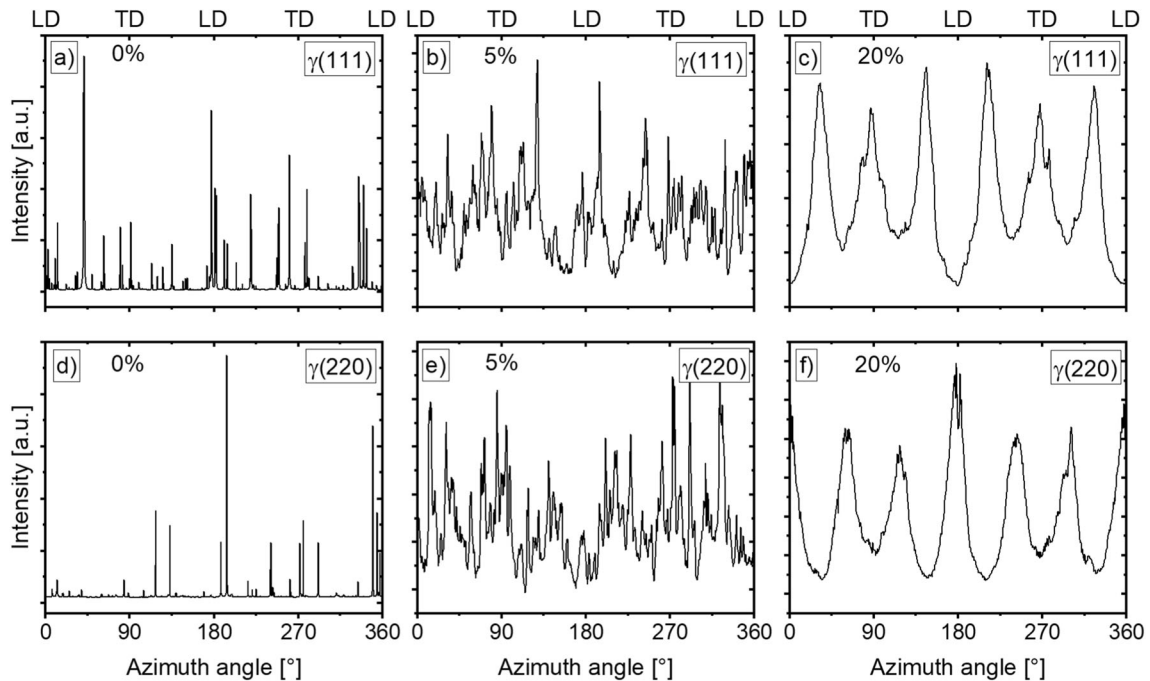


Fig. 4—Unrolled γ -(111) and γ -(220) diffraction rings of VDM® Alloy 780 samples measured at 1000 °C with (a) and (d) before deformation, (b) and (e) at 5 pct deformation, and (c) and (f) at 20 pct deformation. LD: load direction and TD: transverse direction. The absolute intensity scale is different for each diagram.

small amounts of γ' could have precipitated. Forging is performed above the solvus temperature of the hardening phase and below the solvus temperature of the HT phases to maintain formability while preventing grain growth. In the XRD measurements, the HT phases could not be detected; however, this does not exclude that small amounts may have formed. Temperatures of 950, 1000, and 1050 °C were selected to investigate subsolvus forging, forging above the γ' and below the HT solvus, and supersolvus forging, respectively. The stress at which plastic deformation occurs, *i.e.*, the flow stress, decreases with increasing temperature since thermal activation increases at higher temperatures and thus strength decreases. With further deformation, the dislocation density increases, and varying degrees of strain hardening occur for the tested temperatures. At 950 °C, a significant continuous strain hardening with increasing compressive deformation was observed, while hardening is only very slight at 1000 °C and even a softening of the material is observed for deformations of more than approximately 13 pct at 1050 °C. One possible explanation for this behavior is that dynamic recrystallization (DRX) and recovery, both leading to a softening of the material, are more pronounced at higher temperatures. This is corroborated by the decreasing R_q values above about 13 pct deformation in Figure 6, which can also be explained by initiating DRX. Recovery and DRX can also affect the force values of the lower testing temperatures but are not strong enough to lead to an inflection point, *i.e.*, decreasing force values. In their study of supersolvus forging of VDM® Alloy 780, Sharma *et al.* also

observed a stress peak after which the force decreases again due to the combination of DRX and recovery.^[12] Additionally, a peak at small strain levels (yield point phenomenon) that was also found for alloy 718 and alloy 718 plus^[18] is observed for VDM® Alloy 780. The origin of this phenomenon is controversially discussed.^[12] One explanation is related to the drop in stacking fault energy as a result of Co and Nb impeding the slip of partial dislocations. An alternative mechanism explains YPP in terms of the solute atoms blocking the dislocations, resulting in an abrupt increase in stress values.^[12]

2. Microstructure before and during deformation

In the first part of the experiments, *i.e.*, the hot forming, diffractograms were acquired continuously enabling us to follow the formation and development of the crystallographic texture in the VDM® Alloy 780 specimens *in situ* with time and increasing deformation. A vivid way to illustrate the texture development is to show the unrolled Debye-Scherrer rings at different stages of deformation. To facilitate the analysis of the diffraction rings, the rings were unrolled into lines from 0 deg to 360 deg (Y-axis) and the reflections of the γ -phase were identified, as shown at the top of Figure 3. Unrolled diffraction rings are depicted for deformation experiments at 950 °C (Figures 3(a) through (c)), 1000 °C (Figures 3(d) through (f)), and 1050 °C (Figures 3(g) through (i)) before deformation (Figures 3(a), (d), (g)) at 5 pct deformation (Figures 3(b), (e), (h)) and 20 pct deformation (Figures 3(c), (f), (i)). Prior to deformation, only a few

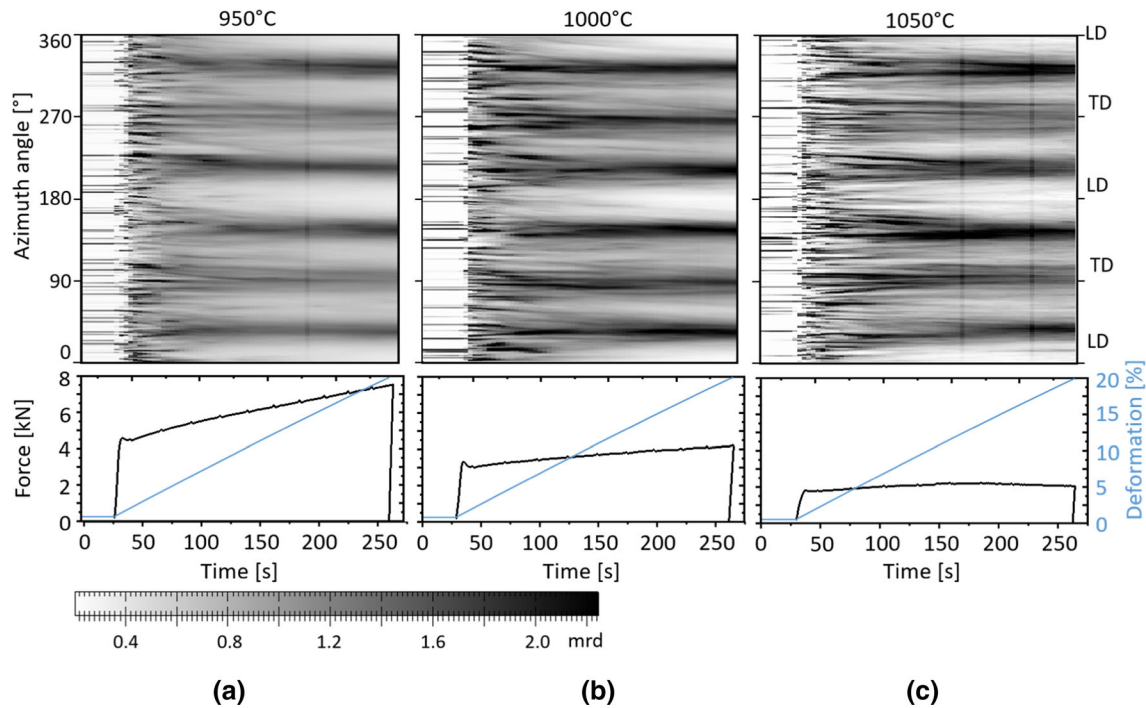


Fig. 5—Azimuth angle vs time diagrams for the γ -(111) reflection during hot compression of VDM® Alloy 780 samples at (a) 950 °C, (b) 1000 °C, and (c) 1050 °C. The distribution of the azimuthal orientation is coded with a greyscale. LD: load direction and TD: transverse direct direction. The process parameters for force and deformation are given below the diagrams.

spots randomly distributed along the rings from individual crystallites occur and no preferred orientation is identified. This is typical for a coarse-grained microstructure and the resulting limited grain statistics. At 5 pct deformation, the rings have become more continuous due to an azimuthally broadening along the ring. The reason for this is the increased crystal mosaicity and the formation of small-angle grain boundaries due to the onset of plastic deformation.^[19,20] By dislocation motion, the grains start to rotate into preferred orientations, which depend on the available slip systems of the phase and the applied stress direction.^[21] This leads to a variation in intensity along the rings, but this is more pronounced after 20 pct deformation (cf. Figures 3(c), (f), (i)), where the deformation texture is visible. Along each ring, six intensity maxima are formed, and for the (311) reflections, there are eight intensity maxima. The intensity maxima of the (111) and (220) reflections are shifted since the (111) reflection has an intensity minimum in the load direction (LD) and a maximum in the transverse direction (TD), contrary to the (220) reflection with an intensity maximum in the LD and a minimum in the TD. An analogous behavior of local minima and maxima distribution is observed for the (111) and (200) reflection vs azimuth angle. The unrolled Debye-Scherrer rings are not perfectly straight lines, this can be explained by a slight variation of the lattice parameters due to different applied stresses in different directions, which is clearer visible at higher 2θ angles. The direction-dependent variation of the lattice parameters is treated later. The evolution of the unrolled diffraction rings is similar for the three temperatures

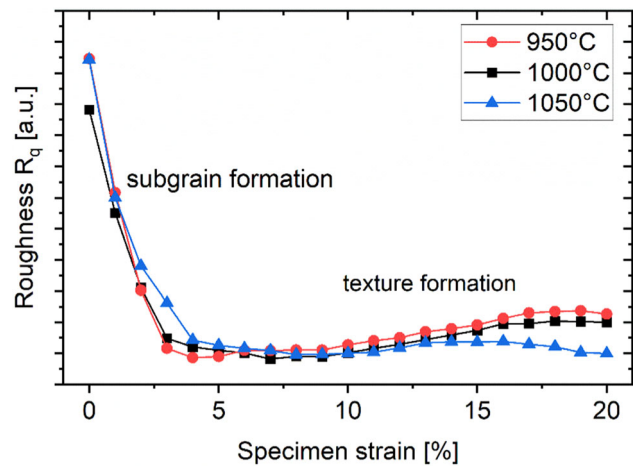


Fig. 6—Evolution of R_q with increasing deformation for the temperatures of 950 °C (red), 1000 °C (black), and 1050 °C (blue). The R_q values are obtained from the intensity values of the unrolled γ -(111) Debye-Scherrer rings (Color figure online).

investigated, showing subgrain formation and the formation of a texture by grain rotation into preferred orientations. However, the forces required for deformation increase significantly with decreasing temperature, as can be seen in Figure 2. Since the γ -(111) reflection together with the γ -(220) reflection clearly shows the microstructural evolution during deformation, unrolled diffraction rings of this reflection are shown in Figure 4. The intensity is plotted against the azimuth angle. Here, one can see again the azimuthal broadening along the

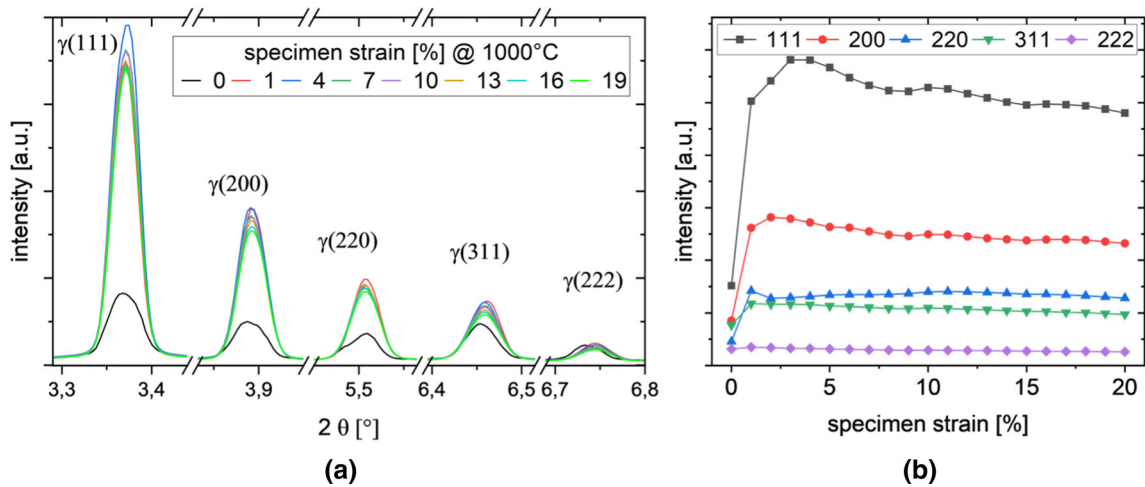


Fig. 7—(a) HEXRD pattern at different deformation stages acquired at 1000 °C and (b) intensity evolution of the different peaks.

ring and the rotation of crystallites, leading to the formation of the texture. To ensure better comparability of the figures, the same deformation stages are used in Figure 3 and in Figure 4. However, Figure 4 only displays the γ -(111) and γ -(220) reflection at 1000 °C, which corresponds to Figures 3(d) through (f). This graph facilitates the localization of the local minima or maxima with higher accuracy and one gets a better impression of the intensity distribution along the ring. Comparing the intensity curves at 5 pct and 20 pct deformation for both investigated lattice planes, the intensity fluctuations at the lower deformation are noticeable, which are caused by individual larger grains still present. In the case of the (111) reflection, the lowest intensity is obtained with the (111) plane normal exactly in load direction (LD), as shown at the top of Figure 4, and corresponds to the following angles 0/360 deg and 180 deg. Several intensity maxima are formed. Two maxima are found for the (111) plane normal in the transverse direction (TD), *i.e.*, at 90 deg and 270 deg in the graph. Four more maxima with slightly higher intensity are found symmetrically at an angle of ± 56 deg to the TD direction, which agrees very well with the results of Yan *et al.* who investigated *in situ* the cold plastic deformation of coarse-grained copper, which has the same crystal structure as the investigated Ni–Co superalloy.^[20] For the (220) reflection, also six intensity maxima form along the ring, with the highest intensity for the two developing in the LD, *i.e.*, 0/360 deg and 180 deg (cf. Figure 4(f)). The other built-up intensity maxima with a slightly lower intensity are formed symmetrically at an angle of ± 63 deg to the LD. The final texture is clearly visible in Figures 4(c) and 5(f). A lot of information can already be gleaned from Figures 3 and 4, but since only individual separate states are shown, few conclusions can be drawn about the progression with time. To show the evolution with time, the individual rolled-up (111) reflection rings were stacked with increasing time, as can be seen in Figure 5.

Liss *et al.* introduced the use of azimuth angle vs time plots (AT plots), where one specific unrolled diffraction ring is repeatedly plotted with time, to visualize the

crystallographic evolution during deformation.^[22]

Figure 5 shows AT plots for the (111)-reflections of the face-centered cubic γ -phase for the three temperatures of 950, 1000, and 1050 °C. The acquisition time for each 2D pattern was approximately 4 seconds, and for each AT plot, 67 diffraction rings were merged to visualize the built-up of texture with time, *i.e.*, increasing deformation. The corresponding force and deformation parameters are displayed below each diagram. The intensities were normalized to multiples of a random distribution (mrd) to enable a quantitative comparison of different AT plots. For example, an mrd value of 1.2 corresponds to an intensity that is 20 pct above, and a mrd value of 0.5 corresponds to an intensity that is 50 pct below the average intensity. In the beginning, *i.e.*, on the left side of the AT plots, discrete horizontal lines are visible corresponding to sharp spots before deformation originating from relatively coarse grains. This is due to a limited number of crystallites. At this stage, the reflections are equally azimuthally distributed and there is no preferred orientation. When deformation sets in approximately after 40 seconds, the single-crystallite reflections broaden azimuthally, due to the creation of subgrains caused by the development of dislocation structures. Thereby the mosaic spread increases and many additional reflections become visible as crystallites which originally had reciprocal lattice vectors lying slightly off the Ewald sphere, move to fulfill the Laue diffraction conditions, and thus reflect.^[20] Some of the initial reflections now move continuously sideways and thus change their azimuth angle with increasing deformation. This change in azimuth angle is caused by grain rotation into the preferred orientation, whereby, symmetrical intensity maxima are formed with the (111) plane normal at approximately ± 56 deg to the TD. These four intensity maxima are also seen in Figure 4(c), and in particular, the exact location of the intensity maxima is more clearly seen in such diagrams. The remaining two maxima are found with the (111) plane normal in TD and are also formed by grain rotation into preferred orientations. It is known that the deformation of grains in polycrystalline face-centered cubic metals, *e.g.*,

Ni-based superalloys, leads to a rotation to activate deformation on the preferred slip systems if the grains are not favorably orientated for deformation.^[23] After 100-150 seconds, *i.e.*, a deformation of approximately 7-11 pct, single grains cannot be separated any longer as the reflections, for the temperatures investigated, merge into continuous Debye-Scherrer rings. Continuous here means that individual spots are no longer discernible; however, a texture is present which manifests itself in intensity variations as a function of the azimuth angle. At 1050 °C, at higher deformation, one observes reflections appearing between the maxima, which can be explained by DRX. This is also confirmed by the decrease in strength (c.f. Figures 2, 5c) and R_q values (c.f. Figure 6) when specimen strains exceed approximately 13 pct deformation at 1050 °C.

3. Intensity distribution along Debye-Scherrer rings—Roughness evaluation

To follow the grain size evolution qualitatively during deformation, the structure of the diffraction rings was further evaluated. Coarse-grained structures lead to single spots on the 2D detector, while fine-grained structures, as obtained by deformation, lead to closed diffraction rings. A measure for the grain refinement is the root-mean-square roughness (R_q), which is obtained from the normalized intensity vs azimuthal angle values of the unrolled diffraction rings (c.f. Equation [1]).

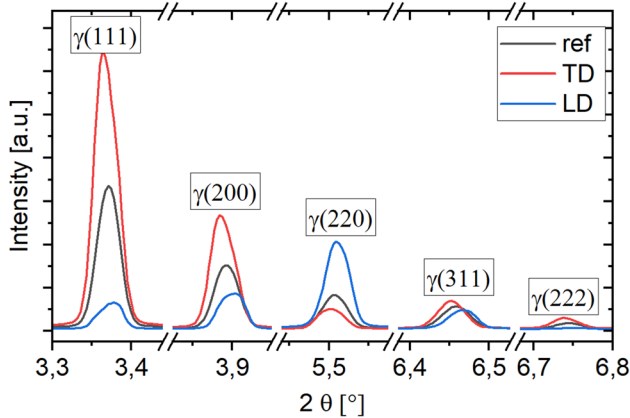


Fig. 8—HEXRD pattern at 20 pct specimen strain acquired at 1000 °C. For the reference (black line), all azimuth angles were taken into account, while for the LD and TD, azimuth angles of ± 5 deg around the respective direction were included.

Freund *et al.* used R_q values as a measure of grain coarsening for polycrystalline Co-based superalloys with increasing temperature.^[16] At low temperatures, a continuous intensity distribution along the Debye-Scherrer rings is observed, *i.e.*, small R_q values which increase when grain growth sets in due to the dissolution of the grain boundary pinning μ -phase.^[16] In this study, the R_q values obtained from the $\gamma(111)$ Debye-Scherrer ring are used to qualitatively show the grain refinement and the development of a texture during the hot forming of the samples. In Section III-B, the R_q values are used to draw conclusions about DRX and precipitation of γ' during cooling.

Before deformation, the specimens exhibit high R_q values at the three temperatures tested, corresponding to a coarse-grained microstructure. When deformation sets in the R_q values for each temperature drop significantly to minimum values at specimen strains of 4 to 7 pct. In the initial state before deformation, there is only a limited number of grains in the illuminated volume, which then increases strongly with deformation, and with it the probability that the Bragg condition is fulfilled. This results in low R_q values and closed diffraction rings. At 950 °C, less deformation is required to get to similar R_q values. However, the behavior of the R_q values at low deformation is very similar. Less recovery occurs at 950 °C and thus subgrain formation is most pronounced at this temperature which explains the faster decrease of R_q at lower temperatures. By further deforming the specimens, the R_q parameter increases again for the three temperatures. This can be explained by grain rotation into preferred orientations, *i.e.*, the built-up of local minima and maxima at certain defined azimuthal angles (c.f. Figure 4(c)). It is important to mention that R_q values are not considered in isolation and that the 2D data are always taken into account, as increased R_q values may result from both grain coarsening or the formation of a texture. The decreasing grain size and the development of a texture influence the R_q value, but in opposite directions. The increase in R_q with increasing deformation due to the formation of a texture is most pronounced at 950 °C and least pronounced at 1050 °C. At 1050 °C, the roughness decreases again for specimen strains exceeding approximately 13 pct since DRX reduces the texture which had developed. When DRX initiates and the newly formed grains are still small, the texture is reduced and so is the R_q value, but as DRX progresses and the grain coarsening associated with it, there is an increase

Table II. 2θ , d -Values, and the Lattice Strain in LD Obtained by Single Peak Fitting of the XRD Pattern of Fig. 7

		$\gamma(111)$	$\gamma(200)$	$\gamma(220)$	$\gamma(311)$	$\gamma(222)$
ref	2θ [deg]	3.37094	3.89292	5.50712	6.45810	6.74436
	d -values [Å]	2.1080	1.8254	1.2906	1.1007	1.0540
TD	2θ [deg]	3.36739	3.88774	5.50244	6.45225	6.73973
	d -values [Å]	2.1100	1.8278	1.2917	1.1017	1.0548
LD	2θ [deg]	3.37410	3.89981	5.51054	6.46620	6.74879
	d -values [Å]	2.1060	1.8220	1.2898	1.0993	1.0533
lattice strain LD vs TD [pct]		- 0.19	- 0.32	- 0.15	- 0.22	- 0.14

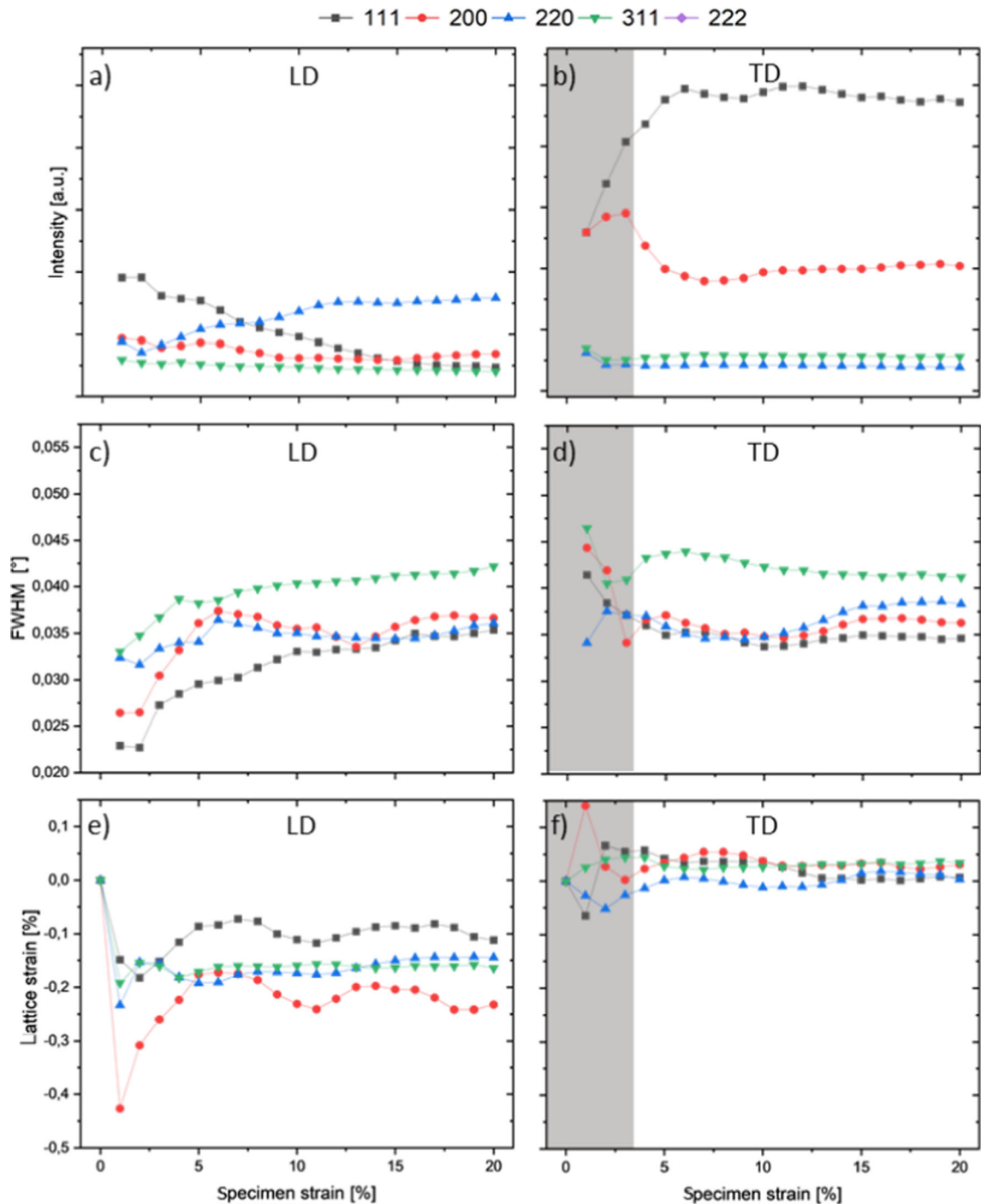


Fig. 9—Evolution of intensity (*a, b*), FWHM (*c, d*), and lattice strain (*e, f*) with increasing deformation in LD (left) and TD (right) at 1000 °C. Shaded areas in TD have been disregarded due to low data quality.

in R_q values again due to the deteriorating grain statistics. The overall evolution of the R_q values is very similar for the temperatures studied, showing subgrain formation as well as the formation of texture with increasing deformation. In the next section, the influence of the hot forming on the microstructure will be investigated by analyzing the diffraction patterns.

4. Evaluation of diffraction patterns

Figure 7(a) shows the diffraction pattern, of the first five γ reflections, obtained at different stages of deformation. To facilitate the readability of the XRD pattern, the individual data points were merged into lines. When comparing the diffraction pattern of the deformed with the reference specimen (strain 0 pct), a pronounced

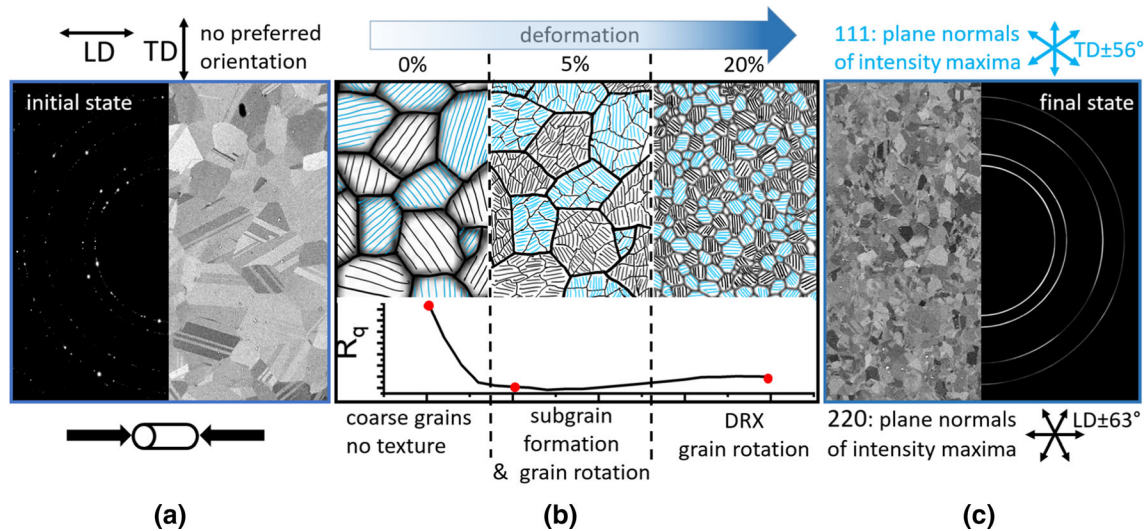


Fig. 10—(a) Experimental results of the initial state, (b) scheme of the microstructural evolution with deformation at 1000 °C, and (c) experimental results after deformation (final state). The blue and black lines intend to show the orientation of the (111) and (220) lattice planes and the red points indicate the R_q values at 0 pct, 5 pct, and 20 pct deformation (Color figure online).

increase in intensity was observed which is quantified in Figure 7(b) by fitting all individual peaks. The fitting was done using a Gaussian profile and least square error minimization. Plastic deformation leads to an increasing number of dislocations and thus to the formation of small-angle grain boundaries. Therefore, the number of coherent scattering regions increases, and with it the probability that the Bragg condition is fulfilled. When comparing the undeformed (black line) to the first deformed (red line), an average increase in the intensity of a factor of approximately 2.7 was observed. This means that the poor grain statistics before deformation hinders the determination of representative intensity values. In addition, the peaks do not show a perfect single peak Gaussian profile shape before deformation, which makes the accurate determination of the most important parameters, *i.e.*, intensity, position, and FWHM, very difficult. After the significant increase in intensity at the onset of deformation, the intensity of the peaks, except for the (220) reflection which remains almost constant, continuously decreases with increasing deformation. The uniaxial compression in our experiments leads to an increased diameter of the cylindrical samples. The increased illuminated sample volume affects the intensity in two ways: on the one hand, the intensity is increased by the larger volume and the resulting increased number of diffraction events. On the other hand, the intensity is attenuated by the larger diameter and the resulting increased absorption. Since the intensity decreases at higher deformation, the higher absorption outweighs the effect of volume increase. In Figure 7, the entire azimuth angle range was included. In the following, the intensity, FWHM, and lattice strain with increasing deformation will be investigated. Since their evolution is anisotropic, these parameters are studied separately for both LD and TD.

The diffraction patterns in Figure 8 show a very strong difference in the intensity and 2θ -position of the

peaks compared to the reference. In the TD, all the peaks except the (220) peak have a higher intensity than the reference which is also seen in Figure 4(f) where the (220) peak has a local minimum in the TD. In contrast, for the LD, only the intensity of the (220) peak increases, which is also in good agreement with Figure 4. This clearly shows the $\langle 110 \rangle$ fiber texture common for fcc alloys under uniaxial compression. For our purpose, the two most important parameters that describe the peaks are the FWHM and the intensity. A change in FWHM can be attributed to changes in the alloy such as crystallite size or microstrain.^[24,25] To affect the FWHM of XRD measurements, the size of the coherent scattering region, however, has to be significantly below 100 nm.^[26] As the γ grains are in the micrometer range, no grain size effects will affect the FWHM, and consequently, varying FWHM values can be directly related to changes in the microstrain. The change in the microstrain can be attributed to an increasing density of both dislocations and stacking faults in the γ grains. In addition, the exact position of the peaks is important, because through them the corresponding lattice plane distances can be calculated. In Table II, the d-values corresponding to the respective reflections were determined according to Bragg's law. Single peak fitting was performed to determine the exact 2θ position (see electronic supplementary Figure S2). The last row of the table quantifies the lattice strain of the LD with respect to the TD.

The different peak positions for the LD compared to the TD are very apparent. As expected, the lattice planes of the peaks with the plane normal in LD are compressed which is expressed in the higher 2θ , *i.e.*, smaller d-values values as compared with the values in TD. The lattice parameters of the reference are averaged over the entire azimuth range and therefore lie between the LD and TD threshold values. Comparing the lattice spacing of LD and TD, the lattice strain in the LD ranges

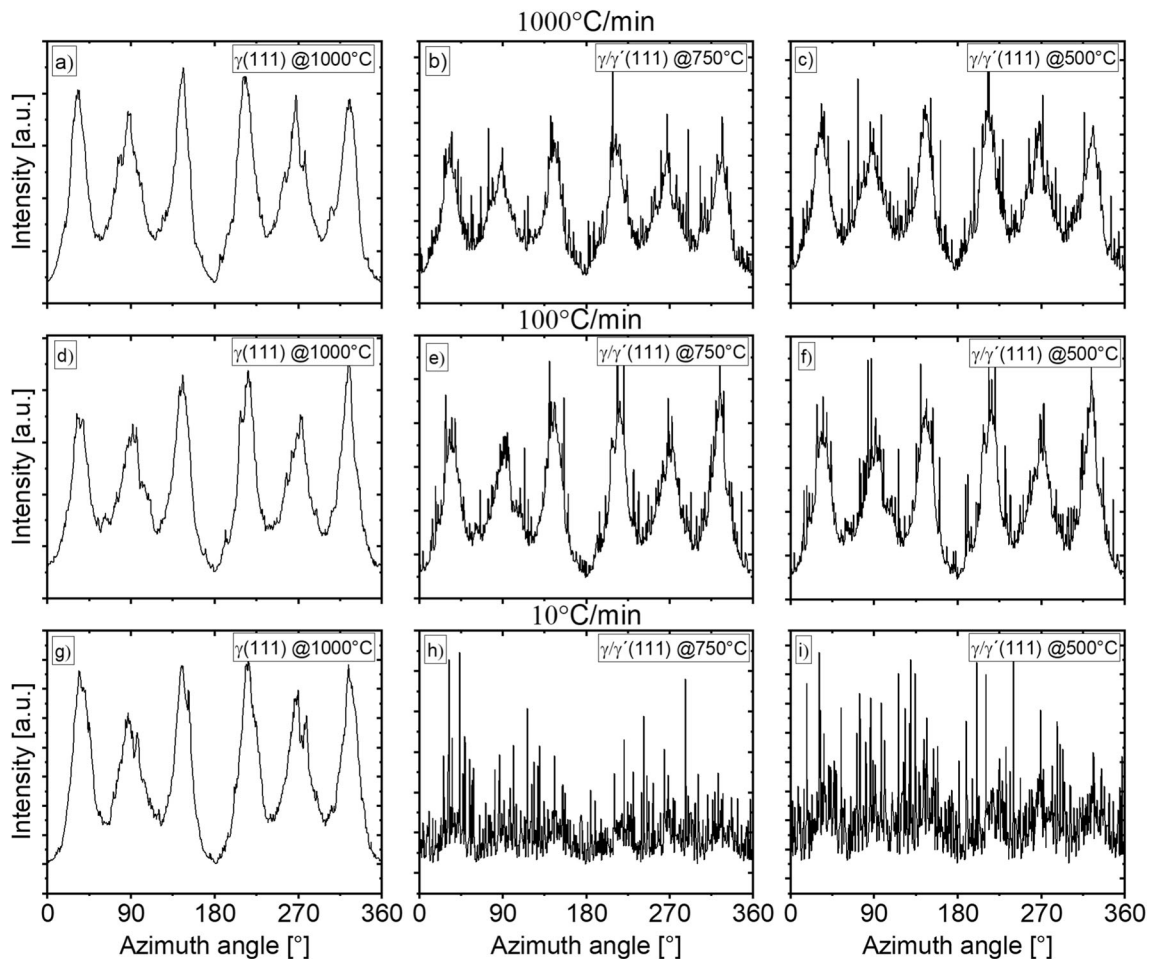


Fig. 11—Unrolled γ/γ' -(111) diffraction rings of VDM® Alloy 780 samples at 1000 °C (a, d, g), at 750 °C (b, e, h), and at 500 °C (c, f, i). In the first line (a-c) a cooling rate of 1000 K/min, in the second line (d-f) a cooling rate of 100 °C/min, and in the third line (g-i) a cooling rate of 10 °C/min were applied. The absolute intensity scale is different for each diagram.

from -0.14 pct and -0.32 pct, which means that the lattice plane spacing of all reflections in LD is reduced. However, the lattice strain is anisotropic. The differences in the lattice strain can be explained by the lattice planes specific elastic constants. Kümmel *et al.* observed similar behavior in their study on the deformation mechanisms in VDM® Alloy 780, where the Young's Modulus in the (200) lattice planes was lowest, and consequently, the lattice strain was highest in this orientation.^[11] The deformation is further facilitated by the higher number of slip systems for the (200) lattice planes. This dependency on Young's Modulus is also seen in our data, with the highest lattice strain for the (200), and the lowest for the (111) and (220) lattice planes. This is the typical behavior of an fcc metal with the highest stiffness in (hhh) and the lowest stiffness in (h00) direction. In the following, the evolution of the intensity, the FWHM, and the lattice strain are analyzed by single peak fitting in LD and TD.

Figures 9(a) and (b) show the intensity evolution with increasing deformation in LD and TD at 1000 °C. The intensities of all reflections except the (220) reflection decrease with increasing deformation in LD. In the *in situ* tensile tests in the study by Kümmel *et al.*, the

intensity behavior was exactly the opposite and only the (220) reflections decreased in intensity, while the other reflections became more intense with increasing deformation.^[11] A possible reason for the opposite behavior is the uniaxial deformation, which was performed in compression in our case and in tension in the study of Kümmel *et al.* The most pronounced intensity gain was observed for the (111) reflection, corresponding to the formation of a $\langle 111 \rangle$ fiber texture, as expected for uniaxial tensile deformation of an fcc alloy.^[11] In the TD, the development of intensity, FWHM, and lattice strain cannot be described so well, because up to a specimen strain of about 3 pct, the peaks cannot be evaluated well due to their irregular shape. Nevertheless, trends can be observed and compared with the behavior in LD. In the TD, there is a very strong intensity increase for the (111) reflection, while in the LD, the intensity decreases for the same reflection which clearly agrees with the anticorrelated local minima and maxima of Figures 4(c) and (f). The intensities of the other peaks remain almost constant during deformation. However, when comparing the intensities in both directions after a specimen strain of 20 pct, all peaks except the (220) show an increased intensity in TD. In LD, the FWHM

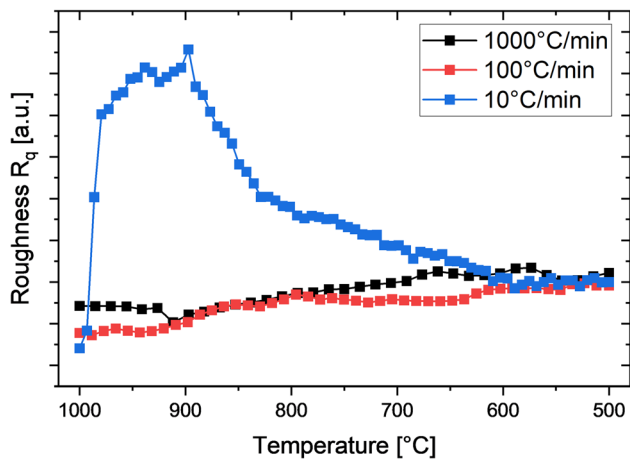


Fig. 12—Evolution of the R_q values for the three different cooling rates shown from 1000 °C to 500 °C. The R_q values are obtained from the intensity values of the unrolled $\gamma(111)$ Debye-Scherrer rings.

of all individual Peaks increases, while the FWHM in the TD remains almost constant with increasing deformation. The (200) and the (220) reflections show an increasing FWHM up to a specimen strain of 6 pct and remain constant up to a specimen strain of 20 pct in the LD. In LD, the lattice planes are compressed which is expressed in the negative lattice strain values. As also seen in Table II, the highest strain values are obtained for the (200) and the (311) reflections in LD; however, in Figures 9(e) and (f), the strain values were normalized to the undeformed specimens, contrary to the values in Table II which are absolute values at this specific deformation state. In TD, the lattice strain values of the (111), (222), and (220) reflections are close to zero, while the (200) and (311) reflections have small positive values indicating slightly increased d-values. The largest lattice strain was observed for the (200) lattice planes. Therefore, during the deformation experiments, the grains in which the (200) lattice planes were orientated with their planes normal in LD were preferred for dislocation activities in the preferred $\{111\} \langle 110 \rangle$ slip system. This can also be supported by comparing the Schmid factors, which indicate the ratio of the actual stress in the slip system to the applied stress. Plastic deformation occurs for suitably oriented grains with high Schmid factors. Since the Schmid factors for grains orientated in the [200] direction are higher than for grains orientated in other directions, these grains deform preferentially.^[11] This enables plastic deformation at lower stress values as compared to the other directions in these grains, which is also known from the literature.^[27] The small positive lattice strain values of the (200) and (311) reflections in TD indicate that these grains experienced a tensile load during deformation. The following Figure 10 is intended to illustrate the microstructural development during deformation according to the XRD data and to show the results shown so far schematically in a diagram.

In Figure 10(b), 3 states, *i.e.*, undeformed, 5 pct deformed, and 20 pct deformed, are selected to describe the effect of deformation on the microstructure at

1000 °C. Furthermore, the initial and final states are shown by a combined SEM and diffraction image. The initial condition is identical to the heat treatment described in Sect. 2, and for the final condition, cooling to RT at 1000 °C/min was performed after deformation. The schematic drawing of the microstructure is intended to illustrate how the microstructure changes with increasing deformation due to subgrain formation, grain rotation, and DRX. However, this is a highly simplified depiction of the microstructure. For a more concise view, only the (111) and (220) lattice planes are shown. The initial state is characterized by grains in the range of 70 μm that are randomly orientated, leading to spotty diffraction rings and very high R_q values. At a specimen strain of 5 pct, the diffraction rings have closed, due to the formation of subgrains and slight changes in the orientation of the subgrains by rotation, but the intensity fluctuations are still strong, indicating still low grain statistics. The subgrains that have formed can be tilted among themselves by a few degrees, as is also shown in Figure 10. Grain rotation into preferred orientations has already started but is not yet far proceeded. Therefore, R_q values are lowest in this range of specimen strain, as the Debye-Scherrer rings have closed, *i.e.*, a relatively constant intensity as a function of the azimuth angle is present, but the texture has not evolved completely. After a height reduction of 20 pct, the diffraction rings show continuous intensity variations due to sufficient grain statistics as a result of DRX and rotation of grains into preferred orientations, *i.e.*, a texture formation. The R_q value has increased due to texture formation. The texture at 20 pct specimen strain features the preferred orientation of the (111) lattice planes in TD and $\text{TD} \pm 56$ deg, while the (220) lattice planes are preferentially orientated in LD and $\text{LD} \pm 63$. This is a characteristic of a $\langle 110 \rangle$ fiber texture, as would be expected with uniaxial compression of fcc alloys. In the next section, the effect of the different cooling rates on the microstructure is shown.

B. Microstructural Evolution During Cooling

After the hot deformation, the specimens were cooled from 1000 °C with three different cooling rates of 1000, 100, and 10 °C/min. As shown in Figure 4, the intensity of unrolled diffraction rings is plotted against the azimuth angle to follow the evolution of the microstructure while cooling.

The conditions after deformation without external force at 1000 °C, *i.e.*, the left row of Figure 11, are very similar, showing the good reproducibility of the experiments, which are identical up to that point. The only difference between the intensity plot of the unrolled diffraction rings of Figures 4(c) and 11(a) is that in the latter the load is removed, and approximately, 30 seconds lie between the acquired diffractograms. No significant change in the microstructure can be observed within this short period. Comparing the evolution of the intensity vs azimuth angle curves at 750 °C, the influence of the different cooling rates becomes obvious. For the fast and medium cooling rates, the texture is still present but single spikes in the intensity show that

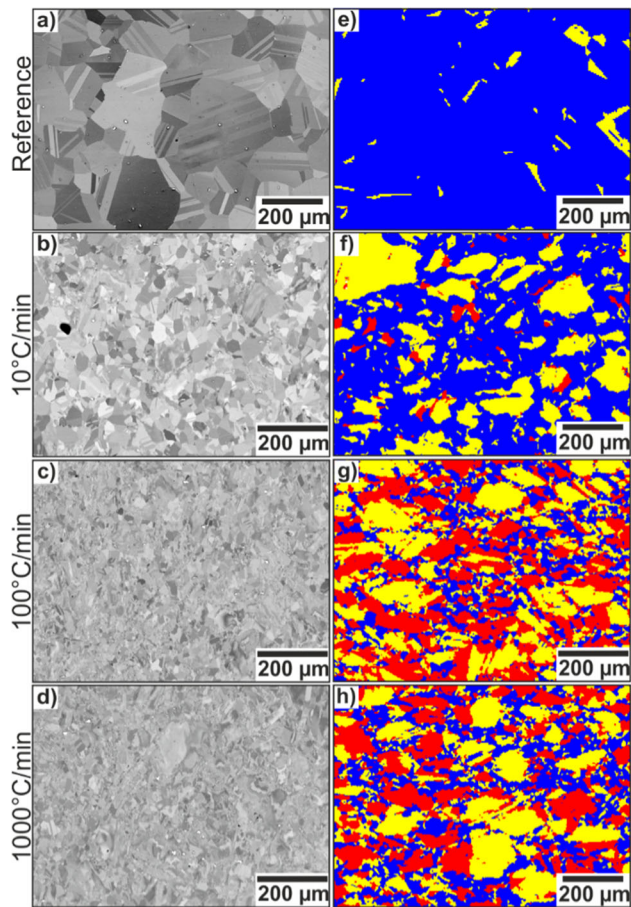


Fig. 13—SEM BSD (a-d) and EBSD recrystallization map (e-h) of samples cooled at different cooling rates after compressive deformation at 1000 °C. The EBSD map shows fully recrystallized (blue), substructured (yellow), and deformed (red) areas (Color figure online).

recrystallization and grain coarsening take place. In the case of slow cooling, the texture is superimposed by many spikes in intensity due to increased recrystallization, which is consistent with prolonged exposure at higher temperatures. At 500 °C and high and medium cooling rates, some additional spikes occur, indicating that further recrystallization took place, but the texture is still strong. It is important to mention that below approximately 970 °C, precipitation of γ' can occur. Since the lattice parameters for the matrix and hardening phase are very similar, it is not possible to distinguish between the γ -(111) and γ' -(111) contributions in the unrolled diffraction rings. The precipitation will be most pronounced at the low cooling rate; however, the precipitation of γ' at the respective cooling rates will be investigated in a separate study. Nevertheless, the spikes in the intensity derive from larger matrix grains, as γ' grains that could have formed are in the nm range. Below 500 °C, no further changes in the microstructure are expected.^[17] At the low cooling rate, the texture is still discernible, but recrystallization is pronounced, reflected in many strong peaks in the intensity curve. This shows clearly how the cooling rate

significantly affects the microstructure and how the texture formed during forging can be largely preserved by rapid cooling. Figure 12 shows the evolution of the R_q values in the temperature range between 1000 °C and 500 °C for the three cooling rates to track the changes in the microstructure.

The evolution of the R_q values with decreasing temperatures is similar at medium and fast cooling rates, but very different compared to the behavior at low cooling rates. Recrystallization, grain growth, and precipitation of the γ' phase can influence the roughness values. The recrystallization will reduce the R_q values as long as the grains formed are small, since the texture will be reduced. When the grains further grow the reduced grain statistics lead to increasing R_q values. In the beginning of the experiment with the slow cooling rate, the strong recrystallization and grain coarsening led to a significant increase in R_q values. The maximum R_q values are reached at approximately 900 °C. Below 900 °C the roughness values decreased, to find a steady state at approximately 600 °C. Interestingly, the temperature of decreasing roughness values coincides with the expected temperature range of γ' precipitation. Precipitation of the hardening phase will not affect the roughness when the precipitates are coherently embedded in the matrix. However, if precipitation of γ' occurs at the grain boundaries or in deformed, *i.e.*, non-recrystallized grains, the R_q values could reduce as these precipitates have no defined orientation. Defects such as dislocations or grain boundaries were found to reduce the precipitation temperature as they act as heterogeneous nucleation sites.^[28] Therefore, nucleation of γ' is facilitated at such sites. This could be the reason why the R_q values decrease significantly in the temperature range of γ' precipitation. For the medium cooling rate, recrystallization and grain growth lead to a slight increase in the R_q values up to approximately 800 °C. Below 800 °C, there is a slight reduction of the R_q values to approximately 650 °C which could also be due to precipitation of γ' . At the highest cooling rates, the R_q values exhibit the smallest variations. This was to be expected since rapid cooling provides the microstructure with the least time for changes. All processes that lead to changes in roughness, such as grain growth or precipitation, are least pronounced here. This shows that R_q values are well suited to observe changes in the microstructure. However, similar R_q values do not mean that the 2D images on the detector will look comparable, as can be seen in Figure 12 at 500 °C, where comparable R_q values are obtained despite vastly different intensity profiles. This once again underlines the importance of using roughness values as a complement to diffractograms and not as an isolated criterion for microstructure evolution. Supplemental microscopic studies were performed to corroborate the diffraction data. To analyze the change in the microstructure depending on the cooling rate after hot deformation at 1000 °C, SEM and EBSD images after the different cooling rates are compared to the reference sample without deformation (c.f. Figure 13). From the SEM images, average grain sizes of 17.9 μm , 15.2 μm , and 14.8 μm were determined for cooling rates of 10 °C/min,

100 °C/min, and 1000 °C/min, respectively. As expected, the average grain size decreases with an increasing cooling rate. The undeformed reference sample has an average grain size of 69.3 μm , not accounting for twins. In the case of fast cooling, the median grain size decreases by a factor of more than four which clearly confirms the proposition of subgrain formation and DRX during deformation made in Section III–A.

The reference sample without deformation is nearly fully recrystallized, while the sample slowly cooled at 10 °C/min has a recrystallized percentage of about 63 pct. The samples cooled at 100 °C/min and 1000 °C/min have similar, but much lower recrystallized percentages between 25 and 35 pct. Due to the faster cooling rates, less time at each temperature is available for further recrystallization and grain growth. From the SEM images seen in Figure 13, the number of grains contained in the *in situ* HE-XRD illuminated volume of 5 mm³ can be estimated. Before deformation, the median grain size is 69.3 μm which leads to approximately 15,000 grains in the 5 mm³ illuminated volumes. The (111) Debye-Scherrer ring shows about 100 spots (counted by zooming in on the raw data), meaning approximately one in 150 grains is oriented in a way that the (111) lattice planes fulfill the Bragg condition and the X-ray hits the 2D detector. The recrystallized grains in the deformed samples show a median grain size of approximately 15 μm which leads to an assumption of approximately 1.5 million grains in the illuminated area. This means approximately 100 times more grains compared to the undeformed sample. The effect is further enhanced by the increased illuminated volume due to the deformation-related larger specimen diameter. This explains the spotty pattern before deformation and why continuous rings form during deformation. With the fastest cooling, the microstructure will be most similar to the microstructure at the end of deformation, as recrystallization and precipitation are less pronounced.

IV. SUMMARY AND CONCLUSION

In this publication, the hot deformation behavior of the new VDM® Alloy 780 was investigated by *in situ* synchrotron-based HE-XRD measurements. The hot forming, for the three tested temperatures of 950 °C, 1000 °C, and 1050 °C, led to subgrain formation and grain rotation into preferred orientations to facilitate deformation along the preferred slip systems. The (111) and the (220) reflections showed an anticorrelated behavior during uniaxial compressive deformation as intensity maxima of the (111) plane normals are found for the TD and intensity maxima of the (220) plane normal in LD, which is characteristic for a $\langle 110 \rangle$ fiber texture. Time-resolved evolution of the microstructure can be seen in the AT diagrams of the (111) reflections, from the initial state before deformation, characterized by coarse, randomly oriented grains, to the final state at 20 pct deformation, in which the grains are smaller and orientated in preferred orientations. The

key mechanisms responsible for the development of the microstructure during deformation are the formation of subgrains, grain rotation, and at higher deformation DRX. The evaluation of the R_q values confirms the results of the unrolled diffraction rings and the evolution of the microstructure in the AT diagrams. Directly after the forging, the effect of the cooling rate on the resulting microstructure was investigated. The slowest cooling rate of 10 K/min leads to pronounced recrystallization of approximately 63 pct and only a slight remaining texture. Contrarily, the higher cooling rates of 100 °C/min and 1000 °C/min where recovery and recrystallization are less effective feature significantly lower recrystallized fractions, and a large part of the texture is retained. Again, the evolution of R_q values allowed a better understanding of the microstructural evolution. It is also worth mentioning that the alloy can be deformed at high temperatures without strong grain growth, although no grain boundary pinning HT phases were detected. This work contributes to a better understanding of the microstructural evolution during the forging process of VDM® Alloy 780, which is of central importance for the further development of this new high-temperature alloy.

ACKNOWLEDGMENTS

Financial support for this work *via* BMBF Projects No. 05K19WO7 and 05K19WEC is kindly acknowledged. This work is based on experiments performed at DESY (Hamburg, Germany). The authors thank the colleagues of DESY for their support during the experiment and data evaluation.

FUNDING

Open Access funding enabled and organized by Projekt DEAL.

CONFLICT OF INTEREST

The authors declare that they have no conflict of interest.

OPEN ACCESS

This article is licensed under a Creative Commons Attribution 4.0 International License, which permits use, sharing, adaptation, distribution and reproduction in any medium or format, as long as you give appropriate credit to the original author(s) and the source, provide a link to the Creative Commons licence, and indicate if changes were made. The images or other third party material in this article are included in the article's Creative Commons licence, unless indicated otherwise in a credit line to the material. If material is not included in the article's Creative Commons licence and your intended use is not permitted by statutory

regulation or exceeds the permitted use, you will need to obtain permission directly from the copyright holder. To view a copy of this licence, visit <http://creativecommons.org/licenses/by/4.0/>.

SUPPLEMENTARY INFORMATION

The online version contains supplementary material available at <https://doi.org/10.1007/s11661-022-06942-5>.

REFERENCES

1. T.M. Pollock and S. Tin: *J. Propul. Power*, 2006, vol. 22, pp. 361–74.
2. D. Furrer and H. Fecht: *JOM*, 1999, vol. 51, pp. 14–17.
3. C. Solís, J. Munke, M. Bergner, A. Kriele, M.J. Mühlbauer, D.V. Cheptiakov, B. Gehrman, J. Rösler, and R. Gilles: *Met. Mater. Trans. A*, 2018, vol. 49, pp. 4373–81.
4. C. Solís, J. Munke, M. Hofmann, S. Mühlbauer, M. Bergner, B. Gehrman, J. Rösler, and R. Gilles: *Miner. Met. Mater. Ser.*, 2019, vol. 2019, pp. 23–32.
5. C. Ghica, C. Solís, J. Munke, A. Stark, B. Gehrman, M. Bergner, J. Rösler, and R. Gilles: *J. Alloys Compds.*, 2020, vol. 814, pp. 152–57.
6. J. Rösler, T. Hentrich, and B. Gehrman: *Metals*, 2019, vol. 9, p. 1130.
7. A. Drexler, B. Oberwinkler, S. Primig, C. Turk, E. Povoden-Karadeniz, A. Heinemann, W. Ecker, and M. Stockinger: *Mater. Sci. Eng. A*, 2018, vol. 723, pp. 314–23.
8. Y. Liu, H. Zhang, Q. Guo, X. Zhou, Z. Ma, Y. Huang, and H. Li: *Acta Metall. Sin.*, 2018, vol. 54, pp. 1653–64.
9. F. Diologent, P. Caron, T. D’Almeida, S. Chambrelan, A. Jacques, and P. Bastie: *Int. J. Mater. Res.*, 2006, vol. 97, pp. 1136–42.
10. A. Bezold, H.J. Stone, C.M.F. Rae, and S. Neumeier: *Metall. Mater. Trans. A*, 2022, vol. 2022, pp. 1–2.
11. F. Kümmel, A. Kirchmayer, C. Solís, M. Hofmann, and R. Gilles: *Metals*, 2021, vol. 11, p. 719.
12. J. Sharma, M.H. Haghighat, B. Gehrman, C. Moussa, and N. Bozzolo: *Superalloys 2020*, Springer, Cham, 2020, pp. 450–60.
13. N. Schell, A. King, F. Beckmann, T. Fischer, M. Müller, and A. Schreyer: *Mater. Sci. Forum*, 2014, vol. 772, pp. 57–61.
14. P. Staron, T. Fischer, T. Lippmann, A. Stark, S. Daneshpour, D. Schnubel, E. Uhlmann, R. Gerstenberger, B. Camin, W. Reimers, E. Eidenberger, H. Clemens, N. Huber, and A. Schreyer: *Adv. Eng. Mater.*, 2011, vol. 13, pp. 658–63.
15. A.P. Hammersley, *ESRF Internal Report* 1997, vol. ESRF97HA02T.
16. L.P. Freund, A. Stark, F. Pyczak, N. Schell, M. Göken, and S. Neumeier: *J. Alloys Compds.*, 2018, vol. 753, pp. 333–42.
17. F. Kümmel, M. Fritton, C. Solís, A. Kriele, A. Stark, and R. Gilles: *Metals*, 2022, vol. 12, p. 1067.
18. A. Momeni, S.M. Abbasi, M. Morakabati, and H. Badri: *Metall. Mater. Trans. A*, 2017, vol. 48, pp. 1216–29.
19. K.D. Liss, A. Bartels, H. Clemens, S. Bystrzanowski, A. Stark, T. Buslaps, F.P. Schimansky, R. Gerling, C. Scheu, and A. Schreyer: *Acta Mater.*, 2006, vol. 54, pp. 3721–35.
20. K. Yan, K.-D. Liss, U. Garbe, J. Daniels, O. Kirstein, H. Li, and R. Dippenaar: *Adv. Eng. Mater.*, 2009, vol. 11, pp. 771–73.
21. L. Margulies, G. Winther, and H.F. Poulsen: *Science*, 2001, vol. 291, p. 2392.
22. K.-D. Liss, T. Schmoelzer, K. Yan, M. Reid, M. Peel, R. Dippenaar, and H. Clemens: *J. Appl. Phys.*, 2009, vol. 106, 113526.
23. S. Biroasca: *IOP Conf. Ser. Mater. Sci. Eng.*, 2015, vol. 82, 012033.
24. N.R. Jaladurgam, H. Li, J. Kelleher, C. Persson, A. Steuwer, and M.H. Colliander: *Acta Mater.*, 2020, vol. 183, pp. 182–95.
25. S.K. Rai, A. Kumar, V. Shankar, T. Jayakumar, K. Bhanu Sankara Rao, and B. Raj: *Scr. Mater.*, 2004, vol. 51, pp. 59–63.
26. H. Chung and D.K. Smith: *Industrial Applications of X-ray Diffraction*, Marcel Dekker Inc., New York, NY, 2000.
27. H.J. Im, S. Lee, W.S. Choi, S.K. Makineni, D. Raabe, W.-S. Ko, and P.-P. Choi: *Acta Mater.*, 2020, vol. 197, pp. 69–80.
28. A. Duchaussoy, X. Sauvage, A. Deschamps, F. De Geuser, G. Renou, and Z. Horita: *Materialia*, 2021, vol. 15, 101028.

Publisher’s Note Springer Nature remains neutral with regard to jurisdictional claims in published maps and institutional affiliations.